Microstructure Map for Self-Organized Phase Separation during Film Deposition

Yong Lu, Cuiping Wang, Yipeng Gao, Rongpei Shi, Xingjun Liu, and Yunzhi Wang

Phys. Rev. Lett. **109**, 086101 — Published 20 August 2012

DOI: 10.1103/PhysRevLett.109.086101

Microstructure map for self-organized phase separation during film deposition

Yong Lu[1, 2], Yipeng Gao[2], Cuiping Wang[1], Rongpei Shi[1, 2], Xingjun Liu[1,*‡], Yunzhi Wang[2,*†]

[1]*Department of Materials Science and Engineering, College of Materials, and Research Center of Materials Design and Applications, Xiamen University, Xiamen, 361005, P. R. China*

[2]*Department of Materials Science and Engineering, The Ohio State University, 2041 College Road, 477 Watts Hall, Columbus, OH 43210, USA*

Drastically different two-phase microstructures have been reported for alloy epitaxial films, including self-organized nanoscale concentration modulations of vertical and lateral stripes. To understand the disparity of these microstructures we study their formation mechanisms via spinodal decomposition during film deposition with the aid of computer simulations. Based on the simulation results a microstructure map is established that describes relationships among the morphology of self-organized two-phase microstructure, initial alloy composition and deposition rate relative to the phase separation kinetics in the film. Depending on the deposition rate relative to the kinetics of spinodal decomposition in the film, both laterally and vertically modulated microstructures could be obtained.

PACS numbers: 68.55.J-, 64.75.St, 64.75.Yz, 81.15.Aa

Self-organized periodical nanostructures have many advanced applications [1-5]. However, current top-down nanofabrication techniques such as lithography [6] are costly and time-consuming. Experimental studies have demonstrated a rich variety of self-organized nanoscale concentration modulations (CMs) in alloy epitaxial films deposited by molecular beam epitaxy (MBE) and by metal-organic chemical vapor deposition (MOCVD), including vertical column structure (perpendicular to the substrate) with lateral concentration modulations (LCMs) [7-14], horizontal layer structure (parallel to the substrate surface) with vertical concentration modulations (VCMs) [15-19], and randomly oriented interconnected two-phase mixtures [20, 21]. If the spatial arrangement and periodicity of these self-organized

CMs could be controlled precisely, these film deposition techniques could be a more efficient alternative for the fabrication of metamaterials [1-6] and semiconductor devices [22].

Many mechanisms have been proposed for the formation of these self-organized CMs. For example, the lateral superlattice structures observed in several III-V semiconductor layers have been attributed [16, 23] directly to stress-driven surface reconstruction. The elastic stress between the substrate and the film has also been suggested [24] as the cause of the preferred LCMs. However, a recent study [25] showed that the elastic interactions are not strong enough to lead to either the LCMs or the VCMs.

Spinodal decomposition in thin films can certainly lead to periodical nanostructures [26-28]. During film deposition, spontaneous spinodal decomposition has been shown to lead to either LCMs [29] or VCMs [30]. However, a comprehensive model that can predict LCM and VCM microstructures observed in experiments as function of materials parameters and processing conditions seems still lacking. In this letter we examine the mechanisms and analyze the conditions for the formation of these self-organized LCMs and VCMs during film deposition. We develop a phase-field model of spinodal decomposition in epitaxial films during a layer-by-layer deposition process to investigate systematically material and processing parameters on the development of CMs in a growing film. With the aid of computer simulations, we establish a microstructure map that describes relationships among morphologies of the self-organized two-phase microstructures, alloy composition and deposition rate relative to the phase separation kinetics. The microstructure map indicates that, within a limited initial composition range, LCMs develop at slow deposition rate relative to the phase separation process in the film. When the deposition rate increases, the film morphology changes gradually from the LCM to a well-developed VCM structure. When the deposition rate is much faster than the phase separation process, a randomly interconnected two-phase microstructure develops.

For simplicity we consider an A-B binary system with a miscibility gap. Assuming no coherency strain energy in the system, the total free energy of the system can be formulated on the basis of the gradient thermodynamics [31]:

$$F = \int_V \left\{ f\left(c(\mathbf{r})\right) + \frac{\kappa}{2}\left[\nabla c(\mathbf{r})\right]^2 \right\} \mathrm{d}\mathbf{r} \qquad (1)$$

where $f(c(\mathbf{r}))$ is the local chemical free energy, $c(\mathbf{r})$ is concentration and κ is the gradient energy coefficient. $f(c(\mathbf{r}))$ is approximated by a double-well function with the equilibrium concentrations of the two co-existing phases being 0 and 1, respectively, e. g., $f(c)=f_0c^2(1-c)^2$, where f_0 is a constant.

The temporal evolution of the concentration field is governed by the Cahn-Hilliard equation [32]. The deposition process is simulated by layer-by-layer growth of the film, i.e., adding an ultra-thin layer with a thickness of l_0 (one grid) and having an average composition of c_0 onto the surface of the existing film in a small time interval ($N\Delta t^*$) at a constant deposition rate, which is defined as $v^*= 1/(N\Delta t^*)$, where N is the number of time iterations between two consecutive layers added and Δt^* is the dimensionless time step. Concentration fluctuations in the newly deposited fresh layers are considered by adding the Langevin noise term in the Cahn-Hilliard equation. A two-dimensional (2D) system is considered, which contains 256 grid points (i.e., 256 l_0) in the horizontal direction and up to $128l_0$ in the vertical direction. Periodical boundary condition is used in the horizontal direction and zero-flux boundary condition is used at both the film surface and the film/substrate interface where no mass exchange is allowed [33, 34]. The deposition process starts with a film thickness of $h=l_0$ and ends with a film thickness of $h=128l_0$. In all the simulations the dimensionless grid spacing is chosen to be $\Delta x/l_0=\Delta z/l_0=1$ and the time step Δt^* is chosen to be 0.01. The dimensionless gradient energy coefficient is chosen as $\kappa^*=1$.

In the following simulations, the average film composition is assumed to be $c_0=0.5$. The temporal evolution of concentration modulation in the film with a deposition rate of $v^*=0.2$ is shown in Fig. 1(a). At the beginning of deposition, CMs within the film tend to develop mainly along the horizontal direction (see the bottom of the film shown in Fig. 1(a) at $t^*=200$) and a "chessboard-like" microstructure emerges (see the circle in Fig. 1(a)). As the film further grows, a VCM structure develops gradually and it is stable till the end of the deposition process at $t^*=640$. After annealing for additional 3.6×10^4 time steps, the horizontal stripes are retained.

Figure 1(b) shows the temporal evolution of concentration modulation in a film deposited at a much slower rate ($v^*=0.053$). In this case, the CM in the film seems to have already well

developed before a new layer is added by the deposition process. As the film grows, a vertical column structure with LCMs appears.

Figure 2 shows comparison among the self-organized microstructures obtained at different film deposition rates with an additional annealing for $3\times10^4\Delta t^*$ after deposition. It can be readily seen that the microstructure could be tailored easily by changing the deposition rate. In the extreme case of high deposition rate (e.g., v^*=0.5), the growth of the film is much faster than the decomposition process and the microstructure developed in the film is similar to those obtained via spinodal decomposition during post-deposition annealing of a homogeneous film. As the deposition slows down (e.g., v^*=0.2), a VCM structure appears. The transition from VCM to LCM seems to occur at $v^* \sim 0.125$. At v^*=0.125, the system will eventually evolve into a LCM structure, but has a rather thick transient layer as shown in Fig. 2(c), which can be characterized as neither LCM nor VCM structures. Such a transient layer becomes thinner when the deposition rate becomes slower. An LCM structure without transient layer is obtained when the deposition rate is reduced down to $v^* \sim 0.053$.

These simulation results show that the relative deposition rate plays a critical role in controlling the self-organized morphological patterns generated by spinodal decomposition during film deposition. In addition, additional simulations show that the self-organized VCMs and LCMs only exist in a rather narrow region of initial composition ($\sim0.4< c_0 <\sim0.6$ in 2D) where the differences between the phase fractions of the two co-existing phases are relatively small. When this difference is large, the minority phase will form discrete particles. In order to illustrate clearly the initial growth conditions (alloy composition, deposition temperature and rate) required for the fabrication of different types of CMs, a microstructure map of different morphological patterns is established (Fig. 3) based on the simulation results in the space of phase fraction determined by alloy composition (the vertical axis) and the film deposition rate relative to the spinodal decomposition in the film (the horizontal axis).

To characterize the ratio of the deposition rate of the film relative to the spinodal decomposition rate within the film, we have used a ratio between the characteristic time of spinodal decomposition and the characteristic time of deposition. The deposition time needed for a layer thickness of λ_{max} is λ_{max}/v, while the time required for the development of a

concentration modulation with λ_{max} is proportional to $\lambda_{max}^2/\tilde{D}$, where $\lambda_{max} = 2\sqrt{2}\pi\sqrt{-\kappa/f''}$ is the wave length of spinodal decomposition that has the maximum growth rate, f'' is the second derivative of the local chemical free energy in Eq. (1) with respect to concentration, and $\tilde{D}$ is the chemical diffusivity. The normalized deposition rate could then be given by the ratio of these two characteristic times: $v^N = v/\left(\tilde{D}/\lambda_{max}\right)$, which is used as the horizontal axis of the microstructural map shown in Fig. 3.

From Fig. 3 one can easily find conditions for desired film morphologies (VCM, LCM, or randomly interconnected microstructure). These predictions agree well with the experimental observations available for InGaP [13, 35, 36], GaAsSb [10, 36, 37] and InAsSb [17, 36] (According to Ref. [38], $\tilde{D}$ is assumed to be 5.2×10^{-19} m^2/s at the growth temperature) and ZnSeTe [18, 39, 40] systems.

The formation of the LCM and randomly oriented interconnected microstructures at the two extreme cases shown in Fig. 2 are readily understood. At the slowest deposition rate (v^*=0.053), spinodal decomposition occurs much faster than the deposition process. When the film thickness is smaller than the critical wavelength of spinodal decomposition ($\lambda_c = \frac{\sqrt{2}}{2}\lambda_{max} = 2\pi l_0$ in the present work), concentration modulations along the vertical directions cannot develop and only LCM structures are formed at the initial stages. Because of the slow deposition rate, the newly deposited fresh layers are always in contact with well-decomposed existing layers within which the A-rich and B-rich regions have already reached concentrations outside the spinodal region and hence there is no up-hill diffusion between the fresh and existing layers (this is in contrast to the case at relatively faster deposition rate that will be discussed below). In this case the morphological pattern developed in the existing layers servers as a template guiding the decomposition of the fresh layers, leading to a LCM structure. At the fastest deposition rate (i.e. $v^* = 0.5$), decomposition during deposition is negligible and the phase separation process is similar to conventional spinodal decomposition in preexisting films.

The formation mechanism of the VCM microstructure at the intermediate deposition rates (v^*=0.2 in Fig. 2) is nontrivial. To analyze the formation process of this microstructure, the detailed microstructural evolution during deposition at v^*=0.2 is shown in Fig. 4. When the film thickness (h) is smaller than the critical wavelength (λ_c) of spinodal decomposition, the concentration modulation could develop only along the horizontal direction as seen in Fig. 4(a). To reveal clearly the formation mechanisms, this simulation was started with a regular CM at the bottom layer. Because of the relatively fast deposition rate, the concentrations of the A-rich and B-rich regions in the decomposing film are still within the spoinodal region. Thus, when a fresh layers is added, the A-rich and B-rich regions beneath simply absorb, respectively, A and B atoms from the freshly deposited layers via up-hill diffusion (but down the chemical potential gradient) as shown in Fig. 5. Then the regions in the freshly deposited layers above the A-rich regions will become A-lean while those above the B-rich regions will become B-lean. As a consequence, a "chessboard-like" structure is developed, as seen in Fig. 4(b), as well as in the circled region in Fig. 1(a). Then the A-rich islands connect with each other and the B-rich islands connect with each other, and the chessboard structure transforms into wavy strips as seen in Fig. 4(c). During further coarsening, the wavy stripes evolve gradually into horizontal stripes. After the horizontal strips have developed, if the newly deposited layer is in contact with a B-rich stripe, then the B atoms in the fresh layer will diffuse into the underneath B-rich stripe via the same up-hill diffusion mechanism. Due to the loss of B atoms in the fresh layer, a new A-rich stripe form over the B-rich stripe as seen in Fig. 4(d). As this process repeats, a VCM structure eventually develops.

Note that only uniform film deposition processes [41] are considered in this letter in which the surface roughness is assumed to be much smaller than the wavelength of concentration modulations developed in the film. In random deposition processes where the surface roughness could be commensurate with or greater than the wavelength of concentration modulations within the film, the effect of surface roughness on the development of different types of spinodal microstructures within the films cannot be ignored. In this case, Monte-Carlo method, which has been used extensively to simulate random deposition processes [42, 43] could be employed, where depositing atoms could occupy randomly lattice sites on top of the film.

In summary, spinodal decomposition during film deposition is simulated using the phase-field method. The effects of the deposition rate, deposition temperature, and alloy composition on the morphology of concentration modulations (CMs) developed in the film are investigated systematically. Based on the simulation results a microstructure map is constructed that predicts different CMs observed in experiments. Such a microstructure map could be useful in guiding the choice of alloy chemistry and deposition conditions to obtain a desired self-organized two-phase microstructure in thin films.

The authors thank Dr. N. Zhou at OSU for useful discussions and acknowledge the supports of Ministry of Science and Technology (2009DFA52170), National Natural Science Foundation (51031003 and 50971109) and Scholarship Council (2010631057) of China (Y. Lu, C. Wang and X. Liu), and the supports of NSF under grants DMR1008384 (Y. Gao and Y. Wang) and AFOSR under grant FA9550-09-1-0014 (R. Shi and Y. Wang).

*Corresponding author:

† wang.363@osu.edu

‡ lxj@xmu.edu.cn

[1] U. Leonhardt, Science **312**, 1777 (2006).

[2] W. Cai *et al.*, Nature Photonics **1**, 224 (2007).

[3] J. B. Pendry, Phys. Rev. Lett. **85**, 3966 (2000).

[4] M. L. Povinelli *et al.*, Appl. Phys. Lett. **82**, 1069 (2003).

[5] N. Liu *et al.*, Nature Materials **7**, 31 (2007).

[6] A. Boltasseva, and V. Shalaev, Metamaterials **2**, 1 (2008).

[7] P. MPetroff *et al.*, J. Cryst. Growth **46**, 172 (1979).

[8] F. Peiro´ *et al.*, Appl. Phys. Lett. **66**, 2391 (1995).

[9] S. W. Jun *et al.*, Appl. Phys. Lett. **68**, 3443 (1996).

[10] V. Fink *et al.*, Appl. Phys. Lett. **79**, 2384 (2001).

[11] S. Francoeur *et al.*, Appl. Phys. Lett. **80**, 243 (2002).

[12] T. Seppa□nen *et al.*, J. Appl. Phys. **97**, 083503 (2005).

[13] J. R. R. Bortoleto *et al.*, Appl. Phys. Lett. **87**, 013105 (2005).

[14] J. R. R. Bortoleto *et al.*, J. Appl. Phys. **101**, 064907 (2007).

[15] G. S. Chen, T. Y. Wang, and G. B. Stringfellow, Appl. Phys. Lett. **56**, 1463 (1990).

[16] A. G. Norman *et al.*, Semicond. Sci. Tech. **8**, S9 (1993).

[17] T. Y. Seong *et al.*, J. Appl. Phys. **73**, 8227 (1993).

[18] S. P. Ahrenkiel *et al.*, Phys. Rev. Lett. **75**, 1586 (1995).

[19] C. Q. Chen *et al.*, Appl. Phys. Lett. **96**, 073103 (2010).

[20] N. A. El-Masry *et al.*, Appl. Phys. Lett. **72**, 40 (1998).

[21] T.-Y. Seong *et al.*, J. Appl. Phys. **85**, 3192 (1999).

[22] T. Mattila, L.-W. Wang, and A. Zunger, Phys. Rev. B **59**, 15270 (1999).

[23] B. A. Philips *et al.*, J. Cryst. Growth **140**, 249 (1994).

[24] K. Y. Cheng, K. C. Hsieh, and J. N. Baillargeon, Appl. Phys. Lett. **60**, 2892 (1992).

[25] D. J. Seol *et al.*, Acta Mater. **51**, 5173 (2003).

[26] A. Boyne, S. A. Dregia, and Y. Wang, Appl. Phys. Lett. **99**, 063111 (2011).

[27] B. S. Guiton, and P. K. Davies, Nat. Mater. **6**, 586 (2007).

[28] S. Hu, Acta Mater. **52**, 3069 (2004).

[29] I. Daruka, and J. Tersoff, Phys. Rev. Lett. **95**, 076102(2005).

[30] K. Fukutani *et al.*, Jpn. J. Appl. Phys. **47**, 1140 (2008).

[31] J. W. Cahn, and H. E. Hilliard, J. Chem. Phys. **28**, 258 (1958).

[32] J. W. Cahn, Acta Metall. **9**, 795 (1961).

[33] A. Novick-Cohen, and L. A. Segel, Physica D **10**, 277 (1984).

[34] C. M. Elliott, and Z. Songmu, Arch. Rat. Mech. Anal. **96**, 339 (1986).

[35] U. Voland *et al.*, Cryst. Res. Technol. **24**, 1177 (1989).

[36] K. Ishida *et al.*, J. Cryst. Growth **98**, 140 (1989).

[37] O. M. Khreis *et al.*, J. Appl. Phys. **84**, 4017 (1998).

[38] R. K. Lal, and P. Chakrabarti, Prog. Cryst. Growth Ch **52**, 33 (2006).

[39] Y. Zhu *et al.*, Comp. Mater. Sci. **50**, 2745 (2011).

[40] Y. Seki and O. Oda, J. Cryst. Growth **179**, 324 (1997).

[41] D. Vogler and P. Doe, Solid State Technol. **46,** 35(2003).

[42] J.W Evans, Phys. Rev. B **39**, 5655 (1989).

[43] F.L. Forgerini and W. Figueiredo, Phys. Rev. E **79**, 041602 (2009).

Figure caption:

Fig. 1 (color online). Temporal evolution of concentration modulations produced by spinodal decomposition during film deposition with a relative deposition rate (in dimensionless unit) (a) v^*=0.2 and (b) v^*=0.053. See text for the definition of v^*. h is thickness of the film and l_0 is the grid size. The circled area in (a) shows a typical "chessboard-like" structure.

Fig. 2 (color online). Simulated microstructures within the film at different deposition rates, obtained after an additional annealing time of $3\times10^4\Delta t^*$ after deposition.

Fig. 3 Phase diagram of morphological patterns showing the dependence of various modulated microstructures on phase fraction (alloy composition) and normalized deposition rate v^N (see text for definition). The dark and light gray areas describe respectively the predicted VCM and LCM microstructural regions. The shaded area between the light and dark gray regions indicates the transition between VCM and LCM microstructures. The open circles are the simulation results and the various solid symbols are the experimental results.

Fig. 4 (color online). Formation sequence of VCM structure simulated by regular CMs at the bottom layer with v^*=0.2.

Fig. 5 (color online). Microstructure (left) and diffusional potential (right) with the flux of B atoms indicated by arrows for early (a) and later (b) stages of VCMs. The diffusion potential is calculated according to $\mu(\mathbf{r})=\partial f/\partial c(\mathbf{r})-\kappa\Delta c(\mathbf{r})$ (see Eq. (1)).

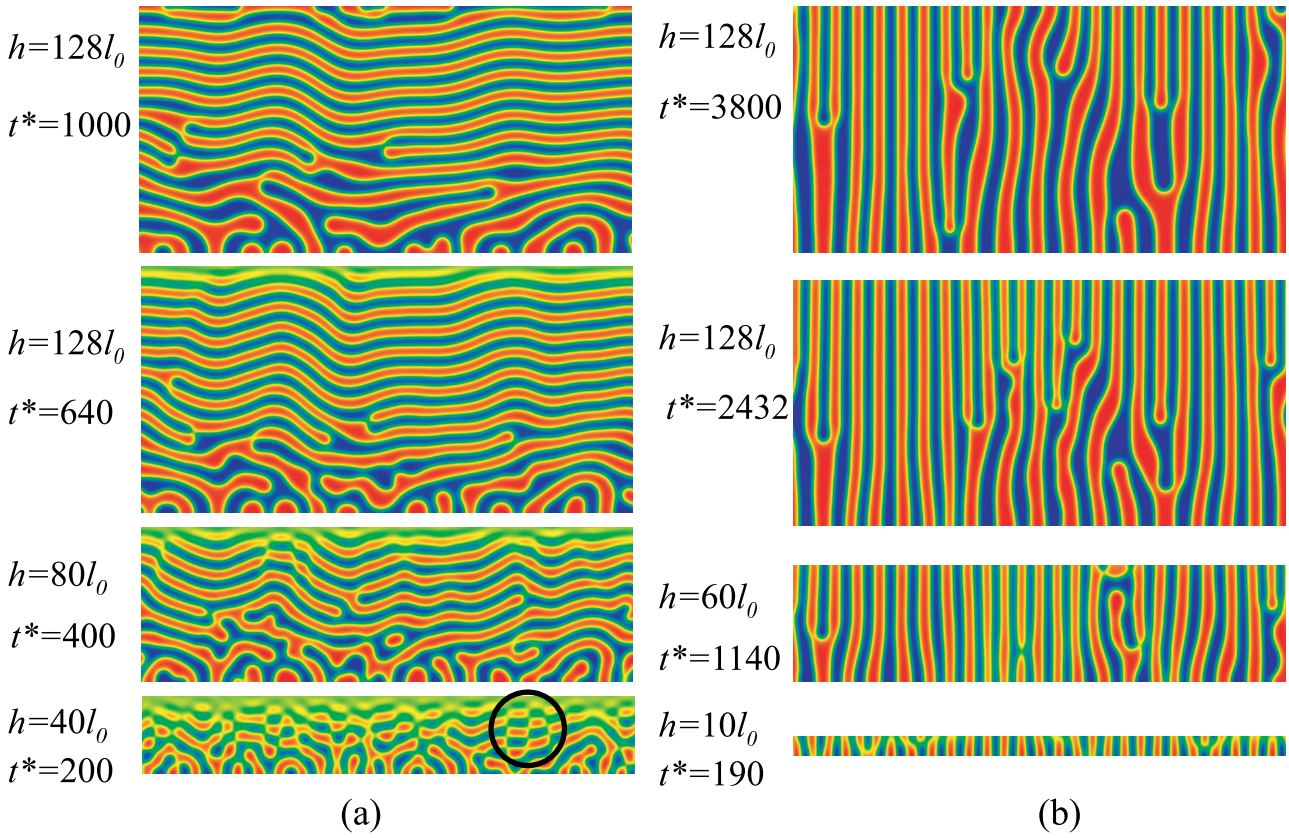

Fig. 1 (color online). Temporal evolution of concentration modulations produced by spinodal decomposition during film deposition with a relative deposition rate (in dimensionless unit) (a) v^*=0.2 and (b) v^*=0.053. See text for the definition of v^*. h is thickness of the film and l_0 is the grid size. The circled area in (a) shows a typical "chessboard-like" structure.

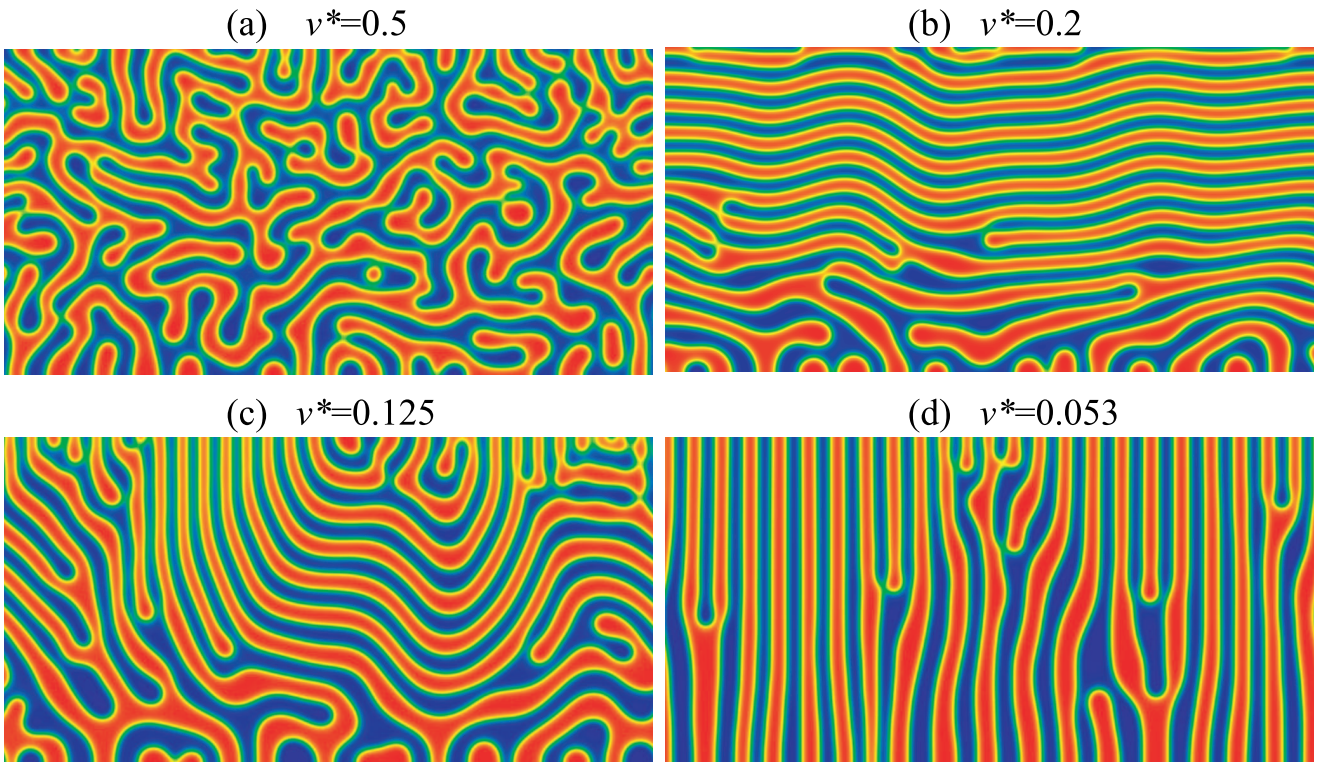

Fig. 2 (color online). Simulated microstructures within the film at different deposition rates, obtained after an additional annealing time of $3\times10^4\Delta t^*$ after deposition.

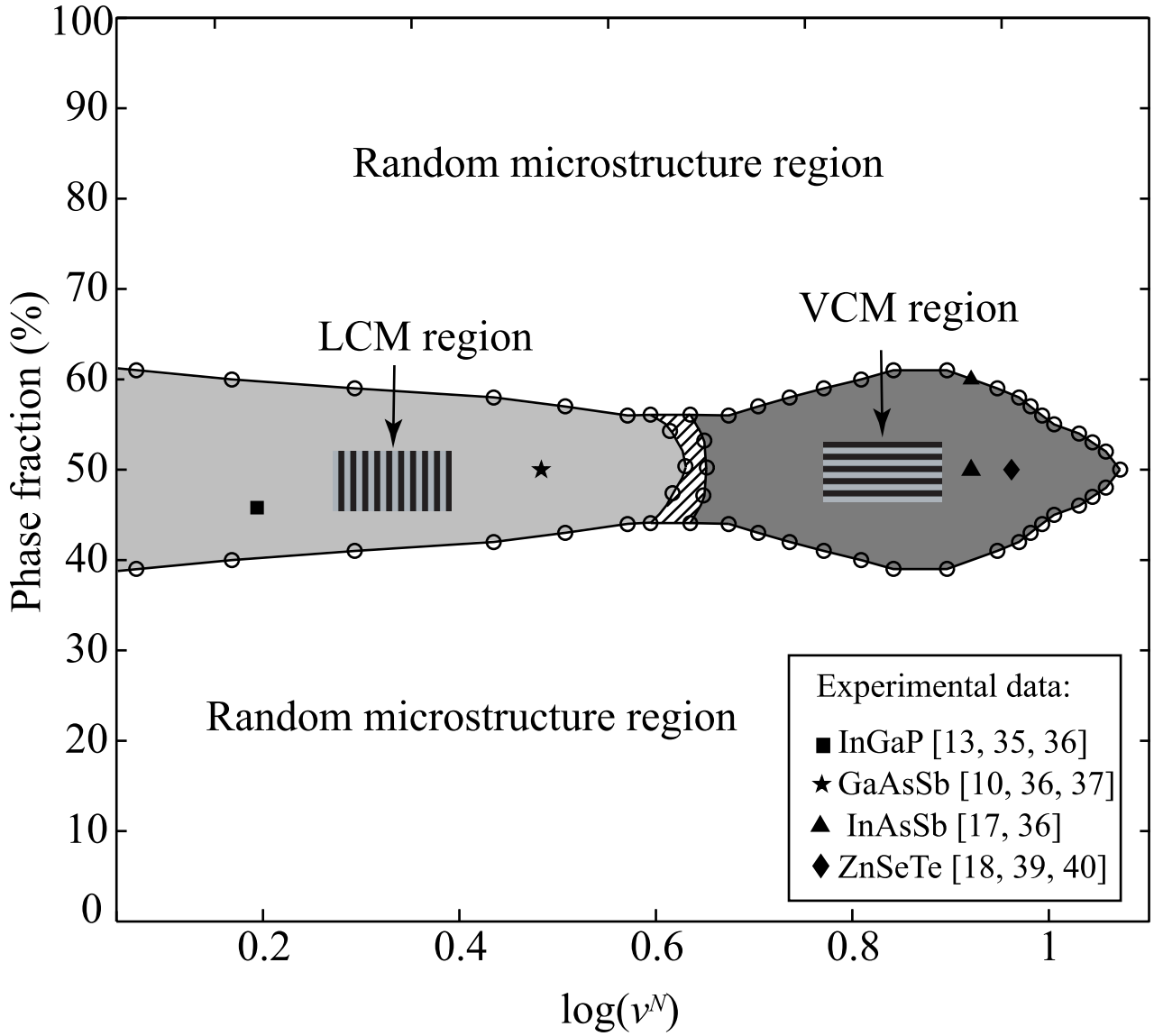

Fig. 3 Phase diagram of morphological patterns showing the dependence of various modulated microstructures on phase fraction (alloy composition) and normalized deposition rate v^N (see text for definition). The dark and light gray areas describe respectively the predicted VCM and LCM microstructural regions. The shaded area between the light and dark gray regions indicates the transition between VCM and LCM microstructures. The open circles are the simulation results and the various solid symbols are the experimental results.

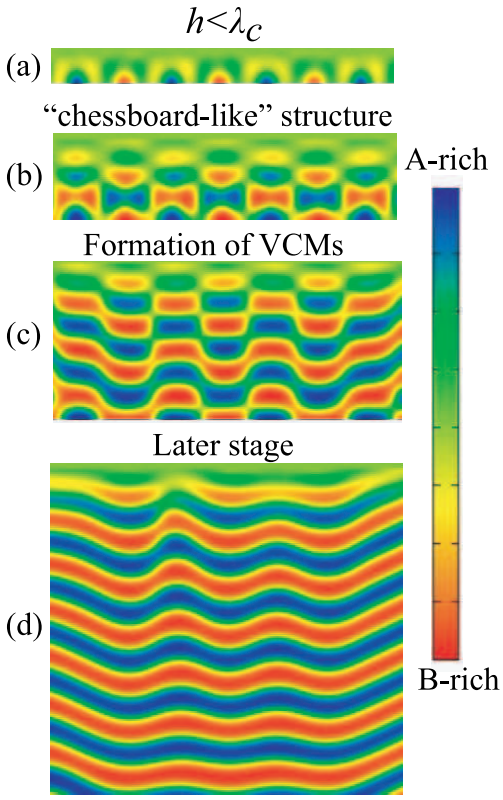

Fig. 4 (color online). Formation sequence of VCM structure simulated by regular CMs at the bottom layer with v^*=0.2.

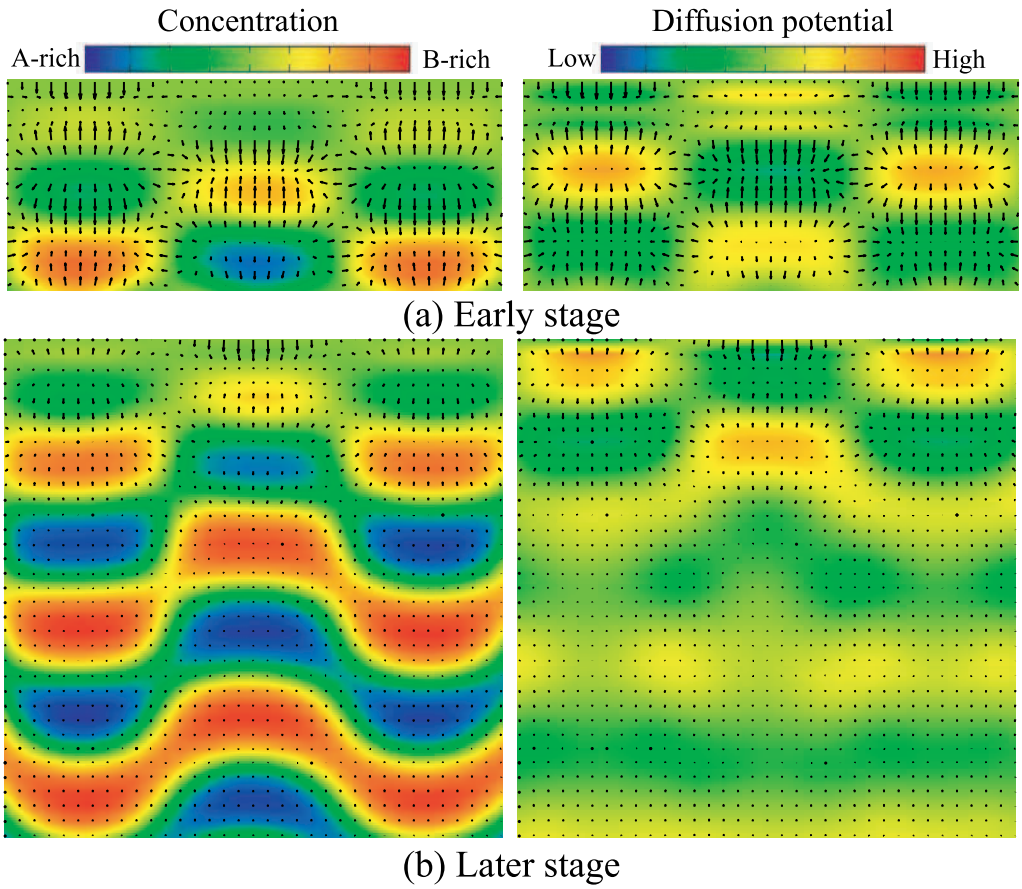

Fig. 5 (color online). Microstructure (left) and diffusional potential (right) with the flux of B atoms indicated by arrows for early (a) and later (b) stages of VCMs. The diffusion potential is calculated according to $\mu(\mathbf{r})=\partial f/\partial c(\mathbf{r})-\kappa\Delta c(\mathbf{r})$ (see Eq. (1)).